Neurocomputing, Vol. 259, 11 October 2017, pp. 201-209
DOI: .1016/j.neucom.2016.07.077

Saliency Driven Vasculature Segmentation with Infinite Perimeter Active Contour Model

Yitian Zhao[a], Jingliang Zhao[a] Jian Yang[a*], Yonghuai Liu[b], Yifan Zhao[c], Yalin Zheng[d], Likun Xia[a] and Yongtian Wang[a]

[a] *Beijing Engineering Research Center of Mixed Reality and Advanced Display, School of Optics and Electronics, Beijing Institute of Technology, China*
[b] *Department of Computer Science, Aberystwyth University, UK*
[c] *EPSRC Centre for Innovative Manufacturing in Through-life Engineering Services, Cranfield University, UK*
[d] *Department of Eye and Vision Science, University of Liverpool, UK*
∗*Email: jyang@bit.edu.cn*

Abstract

Automated detection of retinal blood vessels plays an important role in advancing the understanding of the mechanism, diagnosis and treatment of cardiovascular disease and many systemic diseases, such as diabetic retinopathy and age-related macular degeneration. Here, we propose a new framework for precisely segmenting retinal vasculatures. The proposed framework consists of three steps. A non-local total variation model is adapted to the Retinex theory, which aims to address challenges presented by intensity inhomogeneities, and the relatively low contrast of thin vessels compared to the background. The image is then divided into superpixels, and a compactness-based saliency detection method is proposed to locate the object of interest. For better general segmentation performance, we then make use of a new infinite active contour model to segment the vessels in each superpixel. The proposed framework has wide applications, and the results show that our model outperforms its competitors.

Keywords: Saliency, Retinex, Active Contour, Vascular Segmentation.

1. Introduction

Retinal blood vessels provide useful information for clinical applications, including early detection, diagnosis, and screening of ophthalmological and cardiovascular diseases, and optimal treatment. All these applications require the segmentation of retinal vasculature. In line with the proliferation of imaging modalities, there is an ever-increasing demand for automated vessel analysis systems, for which blood vessel segmentation is the first and most important step. Our application concerns the automated detection of retinal blood vessels in diagnostic retinal images, such as color fundus images and fluorescein angiograms.

The last two decades have witnessed the rapid development of methods for vessel segmentation from different types of medical images, as evidenced by extensive reviews [12, 17, 19]. These include a general review on this topic [17]: a review of 3D vessel segmentation [19]; and a more recent review on segmentation of retinal vessels specifically [12]. Broadly speaking, all established automated segmentation techniques may be categorized as either supervised segmentation [23, 25, 36, 37, 43, 42], or unsupervised segmentation [2, 12, 26, 27, 30, 34, 47, 51], with respect to the overall system design and architecture.

However, the above-mentioned methods still suffer from several major challenges. This is mainly due to the high degree of anatomical variation across the population, and to increasing in complexity of the surrounding tissue/organs. Moreover, artifacts during image acquisition, such as noise, poor contrast and low resolution exacerbate this problem. As a result, it becomes very difficult to choose optimal parameters for a particular segmentation program that will work across a variety of data.

In this paper, we propose a novel infinite perimeter active contour segmentation model hybrid, with salient region detection for segmenting the vessel: a method that is not limited to retinal images, but valid also for images of vessels in other anatomical organs, and so is relevant to many clinical applications. The proposed method consists of three phases: intensity inhomogeneity correction; saliency analysis for initial contour generation; and an infinite perimeter active contour segmentation model with salient region detection.

The contributions of this paper may be summarized as threefold:

1) A Retinex-based inhomogeneity correction method is introduced. The Retinex theory originally dealt with color constancy, which in human vision

ensures that the perceived colors of objects remain relatively constant under varying illumination conditions. However, when extended to vessel image intensity inhomogeneity correction, it has demonstrated good performance and facilitated subsequent processes.

2) A compactness-based saliency analysis of retinal images is proposed, which aims to generate the initial contours for segmentation, leading to more accurate segmentation. It is well established that the saliency information of an image carries the most important features. It emerges from such characteristics in particular image features as visual uniqueness, unpredictability, or rarity, and is often localized to variations in specific image attributes, such as color, gradient, edges, and boundaries [6, 7]. Such attributes are characteristic of vessel-like structures in retinal imagery.

3) The proposed infinite perimeter active contour segmentation model with salient region information is well-suited to most applications related to vascular structures, and in particular to retinal images. It achieves the best performance in comparison studies on four publically available datasets. In particular, it demonstrates better performance in handling small and narrow vessels, even in the case of poor contrast. It has the potential to become a powerful tool for the quantitative analysis of vasculature for the management of a wide range of diseases.

The remainder of this paper is structured as follows. In Section 2, related work relevant to this work is briefly reviewed. Section 3 describes the proposed method in detail. Section 4 and 5 describe the datasets and metrics used for the evaluation, and the experimental results. Section 6 concludes the paper.

2. Related Work

In this section, some background knowledge of related work will be briefly introduced: the classic vessel segmentation models, and relevant work on saliency analysis in medical applications.

2.1. Vessel segmentation

Here, the term *supervised segmentation* we are referring to those methods that use training data to train a classifier (a decision function) so that it can be used for the classification of image pixels in a new, previously unseen image as either part of, or not part of a vessel. Supervised segmentation

requires hand-labeled gold standard images for training. Each pixel is represented by a feature vector, which is obtained from either local or global information derived from the image. The prerequisite for this approach is that a set of features is found that, taken together, provides the necessary discriminative ability to be extracted for training and classification processes. These features can be extracted by different filters: for example, the Gabor filter used in [36]. Various classifiers can be used for the classification tasks, including k-nearest neighbors [37]; support vector machines (SVM) [33, 43]; artificial neural networks (ANN) [35]; Gaussian mixture models (GMM) [25], or Adaboost [23], to name only a few.

In contrast, the term *unsupervised segmentation* here refers to methods that achieve segmentation of blood vessels without using training data or explicitly using any classification techniques [18]. This category includes most segmentation techniques in the literature, such as active contour models [2], wavelets [3], and our proposed new framework. Most unsupervised segmentation methods are filter-based: these techniques are used to enhance the vessels for ease of segmentation. Options include an eigenvalue-based filter [11]; a matched filter [28, 45]; an amplitude-modified second order Gaussian filter [22]; Hessian matrix-based filters [11, 6]; local phase-based filters [18]; multi-scale linear operators [32]; and various wavelet [3, 42] or Gabor filters [36].

A number of active contour models have been proposed for vessel segmentation problems, including the ribbon of twins (ROT) model [2]: geodesic active contour (GAC) model [18]; variations of the active contour without edge model (better known as the CV model [5]) [20, 38, 39, 40, 41, 52]; the infinite perimeter active contour model [4]; and the distance regularization level set evolution (DRLSE) model [21].

2.2. Saliency analysis in medical applications

Research on saliency detection with applications in medical imaging has not been widely exploited [48]. In this section, we review the relevant work on detecting abnormalities in different modalities of medical images by means of saliency information.

Yuan et al. [44] proposed a saliency-based ulcer detection method for use with wireless capsule endoscopy (WCE) diagnosis. It uses a multi-level superpixel representation as the pre-processing phase of saliency detection, and the final saliency map is generated by a fusion strategy of integrating all of the saliency maps obtained at different levels. This method is capable of

accurately representing the contours of ulcerated regions, and these regions are then located by classification tasks. The limitation of this method is that neither its effectiveness nor its promise are well established, because the dataset used for validation is too small. Mahapatra and Sun [24] used the saliency and gradient information in a Markov random field for non-rigid registration of dynamic MRI cardiac perfusion images. This approach attempts to address the problem that most nonrigid registration algorithms fail to give satisfactory results in the presence of intensity changes. Although the saliency detection method provides high quality contrast-enhanced images, the gradient information can still be influenced by noise. For example, this method cannot accurately register the boundary of the left ventricle. A visual saliency-based bright lesion detection method is introduced in [8]. The spectral residual saliency model [14] is employed to compute a saliency map of the color fundus retinal images. The saliency computation obtains a sparse representation of images, and a given image can be classified as normal or abnormal (having bright lesions) by reference to the obtained saliency information. Jampani et al. [16] analyzed the relevance of saliency models in detecting abnormalities in two types of medical images. They extended the Graph Based Visual Saliency (GBVS) model [13] to detect diffuse lesions in chest X-ray images, and high contrast lesions in retinal images. The results were compared with those of three other popular computational saliency models: Itti-Koch [15]; Graph Based Visual Saliency [13]; and Spectral Residual [14]. Most recently, Zhao et al. [50, 49] adapted the saliency concept to detecting abnormalities characteristic of malarial retinopathy (MR). This method not only has the ability to detect three types of leakage (large focal, punctate focal, and vessel segment leakage) in images from eyes with MR, but also is capable to detect the intra-vascular filling defects. However, makes use only of intensity information to generate the saliency map used in the detection process, whose accuracy may therefore be compromised if some normal areas also have high intensities.

3. Methods

The proposed segmentation framework comprises three major steps (each with a distinct component): Retinex-based inhomogeneity correction; compactness-based saliency analysis; and infinite perimeter active contour with hybrid saliency segmentation. Figure 1 shows the overview of the proposed segmentation framework.

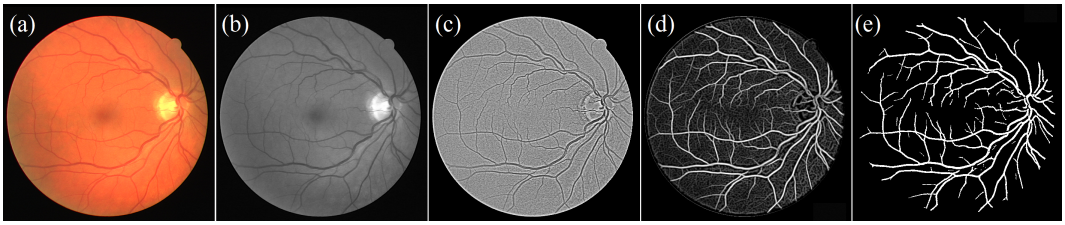

Figure 1: Overview of the main steps of our method. (a) An example image. (b) The green channel of (a). (c) Result after applying Retinex. (d) Result after compactness-based saliency analysis. (e) The proposed segmentation result.

3.1. Retinex-based inhomogeneity correction

Intensity inhomogeneity, often inherited from the image acquisition process, poses a significant challenge to many subsequent image processing tasks. For instance, the retinal images acquired with a fundus camera sometimes exhibit poor contrast, due to too strong or too weak illumination conditions.In this paper, the Retinex theory has been adopted as an effective means of handling these problems. The Retinex theory shows that any given image $\mathbf{I}$ can be modeled as a component-wise multiplication of two components, the reflectance $\mathbf{R}$ and the illumination $\mathbf{L}$: $\mathbf{I} = \mathbf{L} * \mathbf{R}$. Typically, $\mathbf{R}$ reveals the reflectance of the object of interest more objectively, and can thus be regarded as the enhanced image $\mathbf{I}$. A look-up-table log operation transforms this multiplication into an addition, resulting in $i = \log(\mathbf{I}) = \log(\mathbf{L}) + \log(\mathbf{R})$ $= l + r$ [10]. Clearly, the recovery of l or r from I' is an ill-posed inverse image decomposition problem.

To solve this challenging problem, a spatial smoothness constraint is usually imposed. In this work, by contrast, we apply a bilateral filter on Retinex theory to normalize the input medical images [46]. In this paper, a non-local total variation (TV) regularized formulation is adopted on the Retinex theory to normalize the input medical images. The TV regularizer is very effective in recovering edges of images [29]. This phenomenon complements with the PDE-based Retinex method: the reflectance corresponds to the sharp details in the image, and the illumination is spatially smooth. Hence, the regularization can be formulated as a minimization problem, and the non-local TV regularized model for Retinex theory is formed as:

$$\mathbf{R} = \arg\min_{l}\{t\int_{\Omega}|\nabla_w l| + \frac{1}{2}|\nabla(l-i)|_2^2\}, \tag{1}$$

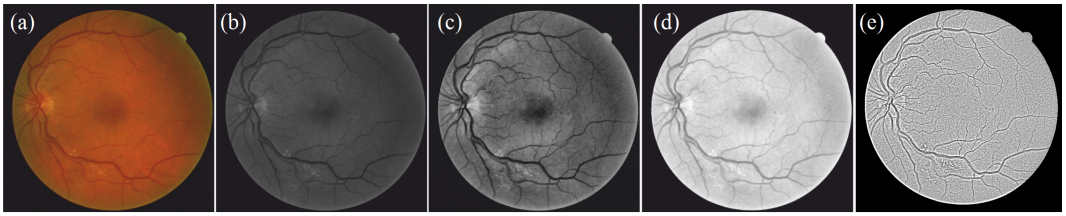

Figure 2: A comparative study of image inhomogeneity correction. (A) An example image. (B) The green channel of (A). (C) Result after applying Histogram Equalization. (D) Result after applying Gamma Correction. (E) Result after applying Retinex.

subject to $l \leq i$. The first term indicates the regularization, and is able to locate and define sharp details. The second term is the L_2 term of the gradient of the illumination: its role is to ensure smooth illumination. The parameter t balances the two terms. Ω is the support of the image. For an image, the non-local weight between pixel $\mathbf{x}$ and $\mathbf{y}$ can be defined as

$$w(x,y) = \exp\Big\{\frac{-K * (l(\mathbf{x}) - l(\mathbf{y}))^2}{2h^2}\Big\}, \tag{2}$$

where K is the Gaussian kernel, and h is the control parameter. By obtaining the non-local weights, the non-local gradient operator at pixel $\mathbf{x}$ can be defined as the vector of all partial difference $\nabla_w l(\mathbf{x}, \cdot)$:

$$\nabla_w l(\mathbf{x}, \mathbf{y}) = (l(\mathbf{y}) - l(\mathbf{x}))\sqrt{w(\mathbf{x}, \mathbf{y})}, \forall y \in \Omega. \tag{3}$$

So the non-local TV regularizer can be defined as

$$\int_\Omega |\nabla_w l| = \int_\Omega \Big(\int_\Omega (l(\mathbf{y}) - l(\mathbf{x}))^2 w(\mathbf{x}, \mathbf{y})\, \mathrm{d}\mathbf{y}\Big)^{\frac{1}{2}}\, \mathrm{d}\mathbf{x}. \tag{4}$$

Figure 2 shows a comparative study of image inhomogeneity correction. It can be seen clearly that Retinex corrects for inhomogeneities more effectively than its competitors: it enhances the contrast between vessels and background more cleanly, and in consequence the vessels are more easily identifiable. Moreover, the optic disk and foveal area are also corrected as well.

3.2. Compactness-based saliency analysis

Intuitively, a human observer perceives only the optic disc regions and vessels as salient regions. Therefore, in this section we advocate the use

of a saliency map for coarse pre-location of the vessel regions. It has been observed that human observers will normally pay more attention to a more compact object than to a more diffuse object. The measure of compactness of an object might therefore be of use as a complementary feature for saliency measurement, with the aim of reducing the number of falsely-detected salient regions.

To measure compactness, the Retinex-processed image is firstly partitioned into Q clusters, $\{\mathcal{C}_1, \mathcal{C}_2, ...\mathcal{C}_Q\}$. After clustering, the compactness of each cluster can be measured. In this framework, The SLIC superpixel algorithm [1] is adopted to replace the rigid structure of the pixel grid. The SLIC is a k-means clustering-based method, and is able to assign pixels to a particular superpixel according to their respective intensities and spatial locations. The superpixel clustering procedure starts with the generation of initial cluster centers. Then a distance measure D to cluster centers for all pixels is defined, with the aim of associating each pixel to its nearest cluster center. The Euclidean distance (d_c) and spatial distance (d_s) are used to define this measure:

$$D = \sqrt{d_c^2 + (\frac{d_s}{S})^2 m^2}, \tag{5}$$

where $S = \sqrt{N/k}$ is the grid interval, k is the desired superpixel number and N is the total number of pixels. m indicates a parameter whose function is to balance the weighting of intensity and coordinates.

For superpixel $\mathcal{P}_j$, its compactness $c(\mathcal{P}_j)$ is defined as

$$c(\mathcal{P}_j) = \exp\Big(- \alpha \frac{\sigma_{x,j} + \sigma_{y,j}}{\sqrt{\mathrm{X}^2 + \mathrm{Y}^2}}\Big), \tag{6}$$

where $\sigma_{x,j}$ and $\sigma_{y,j}$ are the standard deviations of the x and y coordinates of the centroid of the superpixels in $\mathcal{P}_j$, and α is a constant factor that is empirically set to 15. X and Y are the width and height of the input image.

By incorporating the compactness feature with the intensity feature of a given image, the measure of dissimilarity in compactness between $\mathcal{P}_i$ and $\mathcal{P}_j$ can be defined as

$$\begin{aligned} \mathrm{dis}_{compact}(\mathcal{P}_i, \mathcal{P}_j) = \|l(\mathcal{P}_i) - l(\mathcal{P}_j)\| \times \left(1 + \frac{c(\mathcal{P}_j) - c(\mathcal{P}_i)}{2}\right) \\ \times \exp\Big(- \frac{\beta d(\mathcal{P}_j, \mathcal{P}_i)}{\sqrt{\mathrm{X}^2 + \mathrm{Y}^2}}\Big), \end{aligned} \tag{7}$$

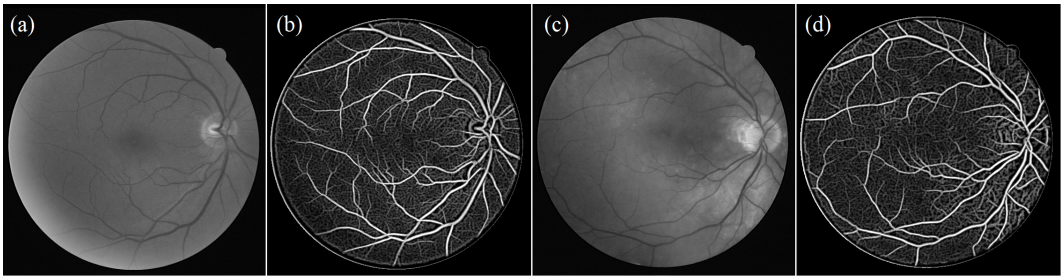

Figure 3: A comparative study of image inhomogeneity correction. (a) and (c): the example images. (b) and (d): the saliency maps of (a) and (c), respectively.

where term $\|l(\mathcal{P}_i) - l(\mathcal{P}_j)\|$ indicates the distinctiveness of the average intensity (l) characteristics of superpixels $\mathcal{P}_i$ and $\mathcal{P}_j$. $d(\mathcal{P}_j, \mathcal{P}_i)$ is the relative average distance of superpixels $\mathcal{P}_j$ and $\mathcal{P}_j$, as proposed in Eq. (3). The constant factor β is empirically set to 300. The larger $\text{dis}_{compact}(\mathcal{P}_i, \mathcal{P}_j)$, the higher the probability that human attention will shift focus from superpixel $\mathcal{P}_i$ to $\mathcal{P}_j$.

Hence, if it is to assist in saliency detection, $\text{dis}_{compact}(\mathcal{P}_i, \mathcal{P}_j)$ should obey the following rules. If $\mathcal{P}_i$ is distinct from $\mathcal{P}_j$, $\text{dis}_{compact}(\mathcal{P}_i, \mathcal{P}_j)$ should be large, and yield a high saliency value for $\mathcal{P}_j$. If $\mathcal{P}_i$ is very similar to $\mathcal{P}_j$, $\text{dis}_{compact}(\mathcal{P}_i, \mathcal{P}_j)$ should be small, and obtain a low saliency value. If $\mathcal{P}_i$ has a high compactness value, the $\text{dis}_{compact}(\mathcal{P}_i, \mathcal{P}_j)$ should be large, suggesting $\mathcal{P}_i$ to be more salient. If $\mathcal{P}_i$ has a low compactness value, the $\text{dis}_{compact}(\mathcal{P}_i, \mathcal{P}_j)$ should be large, showing that $\mathcal{P}_i$ draws less attention (is less salient).

According to Eq. (6), the compactness-based saliency value of $\mathcal{P}_j$ can be written as

$$\text{CS'}(\mathcal{P}_j) = 1 - \exp\Big(- \sum_{j=1, j\neq i}^{n} \text{dis}_{compact}(\mathcal{P}_i, \mathcal{P}_j) \Big). \tag{8}$$

Again, we calculate the final compactness-based saliency value using the mean value of the different superpixel levels: the fusion is also performed pixel by pixel: $\text{CS} = \frac{1}{L} \sum_{l=1}^{L} \text{CS'}$.

Figure 3 illustrates the results of compactness-based saliency maps. It can be seen that the details of the vessels are far more clearly visible when compared to their appearance in original images.

3.3. Saliency-driven infinite perimeter active contour model

In earlier work, a heuristic strategy is commonly used to determine an 'optimal' threshold for segmentation of the enhanced vessel maps [3]. This segmentation is fast, but equally makes generalization of these methods to other applications difficult. In consequence, more robust models such as active contours are to be preferred. The Infinite Perimeter Active Contour (IPAC) model was proposed for the segmentation of objects with irregular boundaries [4]. Denoting a given image by $u_0(\mathbf{x})$, the energy function is given as:

$$\begin{aligned} F^{\mathrm{IPAC}}(\Gamma, c_1, c_2) = \mathcal{L}^2(\gamma - \Gamma) \\ + \lambda_1 \int_{inside(\Gamma)} |u_0(\mathbf{x}) - c_1|^2 \, \mathrm{d}\mathbf{x} \\ + \lambda_2 \int_{outside(\Gamma)} |u_0(\mathbf{x}) - c_2|^2 \, \mathrm{d}\mathbf{x}. \end{aligned} \tag{9}$$

where c_1 and c_2 are the average of $u_0(\mathbf{x})$ inside and outside (Γ) respectively, $\mathcal{L}^2$ is the 2D Lebesgue measure of the γ-neighborhood of the edge set Γ and λ_1 and λ_2 are fitting term parameters.

Inspired by the IPAC model, we propose a novel extension that would integrate hybrid saliency information into the segmentation model. This model considers hybrid region information in an image, such as the saliency map and intensity, in order to achieve reliable segmentation. This model is also effective in detecting vessels mimicking an object with irregular and oscillatory boundaries.

The energy of the infinite perimeter active contour with hybrid saliency model (IPACS) is:

$$F^{\mathrm{IPACS}}(\Gamma, r_n) = \mathcal{L}^2(\gamma - \Gamma) + \sum_{n=1}^{N} \lambda_n S_n, \tag{10}$$

where $\mathcal{L}^2$ is the 2D Lebesgue measure, S_n is the n^{th} region information, and N is the total number of different region terms. Here we consider $\mathcal{L}^2(\gamma - \Gamma) \approx \int_\Omega e^{-(\frac{\phi(\mathbf{x})}{\gamma})^\alpha}$, for a large and even number α, which is an approximation of the γ-neighborhood area in a given image $u_0(\mathbf{x})$.

For this vessel segmentation application, we used the saliency map as the 'vesselness map' v_0 of an image, and the image intensity u_0 as two distinct region terms when in combination serve to extract vessels mimicking an object with irregular and oscillatory boundaries.

Using the Lipschitz level set function, the energy function of our new model can be written:

$$\begin{aligned}
&\min_{\phi(\mathbf{x}),c_1^V,c_2^V,c_1^I,c_2^I} F^{\mathrm{IPACS}}(\phi(\mathbf{x}),c_1^V,c_2^V,c_1^I,c_2^I) = \\
&\mu_1\int_\Omega g(u_0(\mathbf{x}))e^{-(\frac{\phi(\mathbf{x})}{\gamma})^\alpha} + \frac{\mu_2}{2}\int_\Omega (|\nabla\phi(\mathbf{x})|-1)^2\,\mathrm{d}\mathbf{x} \\
&\quad +\lambda_1^V\int_\Omega |v_0(\mathbf{x})-c_1^V|^2 H(\phi(\mathbf{x}))\,\mathrm{d}\mathbf{x} \\
&\quad +\lambda_2^V\int_\Omega |v_0(\mathbf{x})-c_2^V|^2 (1-H(\phi(\mathbf{x})))\,\mathrm{d}\mathbf{x} \\
&\quad +\lambda_1^I\int_\Omega |u_0(\mathbf{x})-c_1^I|^2 H(\phi(\mathbf{x}))\,\mathrm{d}\mathbf{x} \\
&\quad +\lambda_2^I\int_\Omega |u_0(\mathbf{x})-c_2^I|^2 (1-H(\phi(\mathbf{x})))\,\mathrm{d}\mathbf{x},
\end{aligned} \tag{11}$$

where μ_1, μ_2,λ_1^V, λ_2^V, λ_1^I, and λ_2^I are weighting parameters. The parameters λ_1^V and λ_2^V are for the vesselness based term are while λ_1^I and λ_2^I for intensity-based terms. $g(u_0(\mathbf{x}))$ is the edge stopping function. The second term of Eq 11 is introduced for the purpose of distance regularization, as proposed by Li et al. [21].

4. Materials and Evaluation Metrics

Two publically available retinal datasets are used in this work to evaluate the proposed segmentation framework: STARE and DRIVE. **DRIVE**[1] (Digital Retinal Images for Vessel Extraction): consists of a total of 40 color fundus photos, obtained in the course of a diabetic retinopathy screening program in the Netherlands. The images were acquired using a Canon CR5 non-mydriatic 3-CCD camera (Canon, Tokyo, Japan) with a 45 degree field of view. Each image resolution is 768×584 pixels. The set of 40 images was divided into a test and a training set, each containing 20 images. **STARE**[2](STructured Analysis of the Retina) was conceived and initiated at the University of California. This database contains 20 color photographic images of the fundus, 10 of which show evidence of pathology. The digitized slides were captured by a Topcon TRV-50 fundus camera (Topcon, Tokyo, Japan), and the photos were digitized to 605×700 pixels.

[1] `http://www.isi.uu.nl/Research/Datasets/DRIVE/`

[2] `http://www.ces.clemson.edu/~ahoover/stare/`

These datasets were chosen primarily because of the availability of reference standards from manual annotations of the retinal vessels by experts. The segmentation performance is measured by sensitivity (Se), specificity (Sp), accuracy (Acc), and the area under a receiver operating characteristic (ROC) curve, also known as AUC. This measure has the ability to reflect the trade-offs between the Se and Sp. The first three parameters are defined as $\frac{tp}{tp+fn}$, $\frac{tn}{fp+tn}$, $\frac{tp+tn}{tp+fp+tn+fn}$, respectively and $AUC = \frac{Se+Sp}{2}$. tp, tn, fp and fn indicate the true positive, true negative, false positive, and false negative, respectively.

5. Experiments and Results

In this section we present experiments to evaluate the performance of our proposed model.

5.1. Results

In order to establish the effectiveness of our proposed method, we compared its with that of the existing state-of-the-art vessel detection methods on the DRIVE and STARE datasets. The results are shown in Table 1, and the chosen methods have been ordered by the categories to which we assigned them earlier: the most recent six supervised methods [25, 23, 36, 37, 42, 43], and seven unsupervised segmentation methods [2, 3, 26, 12, 27, 30].

Overall, our framework outperforms its competitors, by taking into account both global features of the image through the Retinex analysis, and local features through the compactness-based saliency analysis. The result is that more fine vessels are detected. To be more specific, the sensitivity of the proposed method is in the top two in both the supervised and the unsupervised methods, with $Se = 0.782$, only 0.003 behind the highest performing highest performing supervised method [31]. The specificity, accuracy, and AUC are 0.979, 0.957, and 0.875 respectively, which are also the highest values achieved by any method tested.

The optic disk and foveal area in retinal images frequently result in instances of false detections when analysed by most existing vessel segmentation methods [3, 30]. In this work, after application of the Retinex, the optic disc region has been normalized to a similar level with the background. Therefore, the optic disc will not be misidentified as a vessel after segmentation, a common problem when the Retinex is not used. This implies that

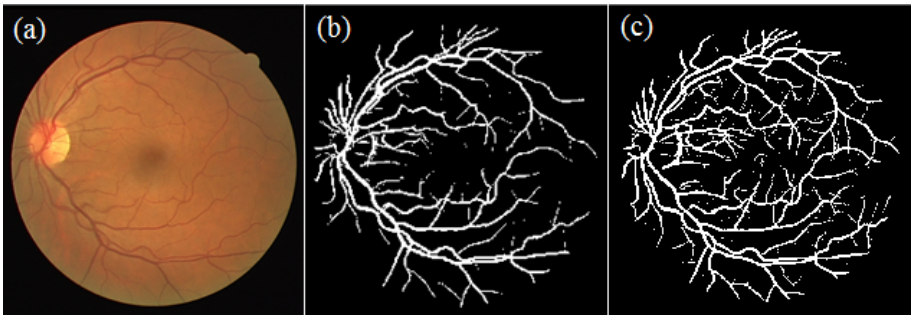

Figure 4: Illustrations of the importance of Retinex based inhomogeneities correction. (a) An example image. (b) IPACHS segmentation result without Retinex applied. (c) IPACHS segmentation result with Retinex applied.

improved specificity values are likely to be seen after the application of the Retinex: and this is confirmed by the scores seen in Table 1.

By contrast, the sensitivity scores are very similar irrespective of the presence or absence of the Retinex. Table 1 also presents the evaluation results in terms of the proposed framework with and without application of the Retinex pre-processing algorithm. This confirms that the Retinex contributes significantly to the final performance results.

In addition, the results of the proposed IPACHS model without Retinex applied are also provided in Figure 4 and Table 1. Usually, the optic disc and foveal area often cause false detections by most existing vessel segmentation methods. In our work, the optic disc region has been normalized to a similar level with the background by applying Retinex, and lead to better segmentation performances: more small vessels have been identified and extracted, and the Se, Sp, Acc, and AUC have raised been 0.022, 0.011, 0.011, and 0.022, respectively, when compared the IPACHS without the Retinex. These scores reinforce the conclusion that Retinex contributes significantly to the proposed segmentation model.

Table 1: Performance of different segmentation methods on the DRIVE and STARE datasets. *Se*: sensitivity; *Sp*: specificity; *Acc*: accuracy; *AUC*: area under curve.

Methods	**DRIVE**				**STARE**			
	Se	Sp	Acc	AUC	Se	Sp	Acc	AUC
Second observer	0.776	0.972	0.947	0.874	0.895	0.938	0.934	0.917
Supervised methods								
Lupascu et.al [23]	0.720	-	0.959	-	-	-	-	-
Marin et.al [25]	0.706	0.980	0.945	0.843	0.694	0.981	0.952	0.838
Orlando et.al [31]	0.785	0.967	-	-	-	-	-	-
Soares et.al [36]	-	-	0.946	-	-	-	0.948	-
Staal et.al [37]	-	-	0.946	-	-	-	0.951	-
Wang et.al [42]	-	-	0.946	-	-	-	0.952	-
You et.al [43]	0.741	0.975	0.943	0.858	0.726	0.975	0.949	0.851
Unsupervised methods								
Al-Diri et.al [2]	0.728	0.955	-	0.842	0.752	0.968	-	0.860
Bankhead et.al [3]	0.703	0.971	0.937	0.837	0.758	0.950	0.932	0.854
Dizdaroglu et. al [9]	0.718	0.974	0.941	0.846	-	-	-	-
Fraz et.al [12]	0.715	0.976	0.943	0.846	0.731	0.968	0.944	0.850
Matinez-Perez et.al [26]	0.724	0.965	0.934	0.845	0.750	0.956	0.941	0.853
Mendonca et.al [27]	0.734	0.976	0.945	0.855	0.699	0.973	0.944	0.836
Nguyen et.al [30]	-	-	0.940	-	-	-	0.932	-
Palomera-Perez et.al [32]	0.660	0.961	0.922	0.811	0.779	0.940	0.924	0.860
IPACHS without Retinex	**0.760**	**0.968**	**0.946**	**0.864**	**0.766**	**0.972**	**0.949**	**0.869**
IPACHS with Retinex	**0.782**	**0.979**	**0.957**	**0.886**	**0.789**	**0.978**	**0.956**	**0.885**

5.2. Effectiveness of vesselness maps

The proposed segmentation model requires a vesselness map, and in this paper a compactness-based saliency map is utilized. In order to demonstrate the importance of the compactness-based vesselness map in the proposed segmentation framework, it has been compared with three vesselness map generators: an eigenvalue-based filter [11], a wavelet-based filter [3], and a local phase-based filter [18]. The parameters recommended in the respective were used. Eigenvalue-based scales: 18, scale ratio: 2; wavelet scales: 23; local phase scales: 23. These parameters may be adjusted to obtain better results according to the nature of the images, but any such adjustment is unlikely to affect the ranking of the overall segmentation model when compared to other state-of-the-art models.

Figure 5 gives an example of the segmentation results. The vesselness maps were generated by the eigenvalue-based, wavelet-based, local phase-based, and the proposed saliency-based filters, respectively. It can be seen that the saliency-based filter is not only sensitive on large vessels, but also exhibits high performance on small vessels, which results in the whole vessel structure standing out more clearly from the background.

The segmentation results derived from these vesselness map are also shown in the bottom row of Figure 5. As expected, the segmentation result based on the proposed saliency-based vesselness map confirms that more vessels are segmented than in the results obtained by the other three methods. Table 2 further confirms this observation. The evaluation of LP in terms of Se, Sp, Acc, and AUC obtains the highest values in each of the three datasets. In addition, the statistical analysis results show that the: Se, Sp, Acc, and AUC values of the saliency-based method are significantly higher than those of the other three filters (all $p < 0.001$).

5.3. Effectiveness of active contour models

In this section, the proposed IPACHS segmentation model is compared with four other active contour models: Chan-Vese (CV) [5], Ribbon of Twins (ROT) [2], distance regularized level set evolution (DRLSE) [9] and infinite perimeter active contour (IPAC) [4]. The CV, IPAC, ROT, and DRLSE segmentation models are implemented as in the original papers. The evaluation results of these models on the DRIVE and STARE datasets are demonstrated in Table 3.

It can be observed from Table 3 that in terms of the Se, Sp, Acc and AUC parameters IPACHS outperforms its competitors on both the DRIVE

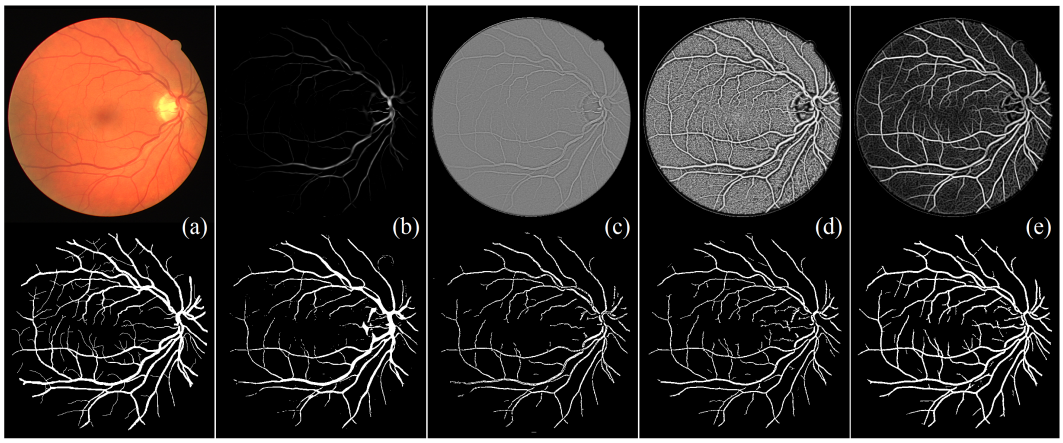

Figure 5: Illustrative vesselness results, using different methods and their subsequent IPACHS-based segmentation results. Top row, (a)-(e): sample image, eigenvalue-based [11], wavelet-based [3], local phase-based [18], and the proposed saliency-based, respectively. Bottom row, (a)-(e): manual annotation of (a), and automated segmentation results (b)-(e), respectively.

and STARE datasets. In particular, the Se, Sp, Acc and AUC of the IPACHS model have the highest scores on the DRIVE dataset: 0.782, 0.979, 0.957, 0.862, and 0.886, respectively. For the STARE dataset, the Se, Sp, Acc and AUC of the IPACHS model also record the highest scores: 0.789, 0.978, 0.956, 0.885 and 0.801, respectively.

6. Discussion and Conclusions

The detection of vessels is usually the first and most important step for automated vessel analysis tools. If a segmentation method cannot handle the relevant image factors, such as intensity, color and local shape effectively, then its performance will be less satisfactory, or at least will not be generalizable to wider applications. For most of the segmentation models [36, 47], vessel enhancement depends on assessment of the intensity parameter only. Such methods may not be able to overcome the degree of intensity variation present in the original image.

In this paper, we have proposed a new framework for the vessel segmentation problem that exploits the advantages of Retinex-based intensity inhomogeneity correction, compactness-based saliency estimation, and an infinite perimeter active contour with hybrid saliency model. Active contour

Table 2: Segmentation performance of different vesselness map estimation methods: (eigenvalue-based. [11], wavelet-based [3], local phase-based [18], and the proposed saliency-based methods).

Dataset	vesselness method	Se	Sp	Acc	AUC
DRIVE	eigenvalue-based	0.686	0.867	0.853	0.776
	wavelet-based	0.716	0.978	0.946	0.848
	local phase-based	0.744	0.978	0.953	0.861
	saliency-based	**0.782**	**0.979**	**0.957**	**0.886**
STARE	eigenvalue-based	0.634	0.967	0.938	0.801
	wavelet-based	0.776	0.954	0.943	0.865
	local phase-based	0.780	0.975	0.951	0.874
	saliency-based	**0.789**	**0.978**	**0.956**	**0.885**

Table 3: Performance of different segmentation models on the DRIVE, and STARE datasets. *Se*: sensitivity; *St*: specificity; *Acc*: accuracy; *AUC*: area under curve.

	DRIVE				STARE			
	Se	**Sp**	**Acc**	**AUC**	**Se**	**Sp**	**Acc**	**AUC**
CV	0.679	0.924	0.939	0.802	0.775	0.950	0.937	0.863
ROT	0.728	0.955	-	0.842	0.752	0.968	-	0.860
DRLSE	0.718	0.974	0.941	0.846	-	-	-	-
IPAC	0.721	0.966	0.944	0.843	0.758	0.964	0.946	0.861
IPACHS	**0.782**	**0.979**	**0.957**	**0.886**	**0.789**	**0.978**	**0.956**	**0.885**

models appear to be a natural choice for automatic segmentation purposes, as they can take into account the geometry information of the object as well as other useful information geometric such as intensity. The proposed framework has been applied to two publicly-available retinal datasets: the results demonstrate that each component of the framework can provide the level of performance expected, and that the overall framework outperforms most existing methods in terms of accuracy and efficiency.

Although in this paper we have evaluated our proposed framework on retinal imagery alone, due to the limited availability of public-access datasets, the method is well suited to address segmentation problems in images of other organs, acquired using different imaging techniques. Figure 6 (b) shows the segmentation result of a fluorescein angiography retinal image (Figure 6 (a))

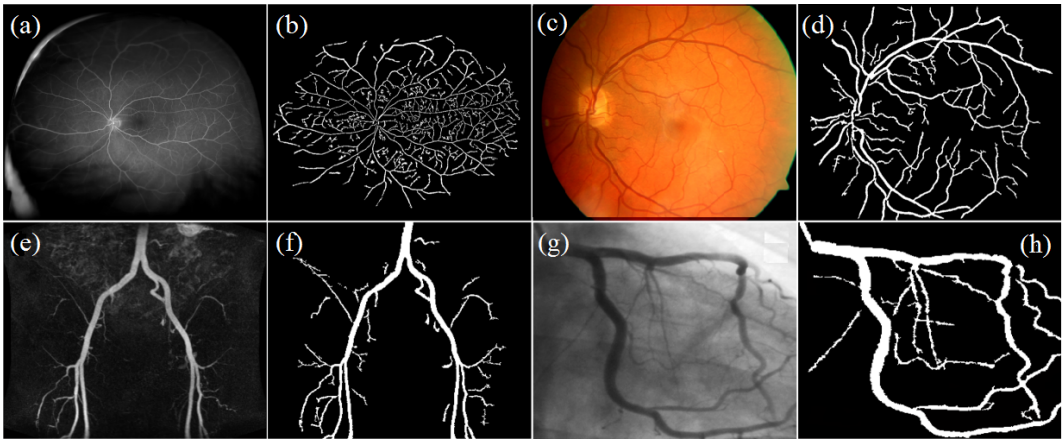

Figure 6: Segmentation results on different imaging modalities. (a) A fluorescein angiogram retinal image from VAMPIRE; (c) A color fundus retinal image with diabetes; (e) A pelvis MRI image; (g) A coronary angiography image; (b), (d), (f) and (h) are the segmentation results of (a), (c), (e) and (g) respectively. (e) and (g) are publically available from http://www.osirix-viewer.com

from the VAMPIRE database[3]. It illustrates that the proposed method can achieve good performance in extracting the vessels from these kinds of retinal images. Figure 6 (d) shows the segmentation results on a retinal image (Figure 6 (c)) from a patient with diabetes, taken from the ARIA dataset. It can be seen that the proposed segmentation method gives a promising result on images of the diseased retina. To demonstrate that our method is applicable to wider applications, we also apply our method to both MRI (Figure 6 (e)) and X-Ray (Figure 6 (g)) images, and the results (Figure 6 (f) and (h)) demonstrate its good performance in detecting thin vessels even in low contrast areas.

In conclusion, in this paper we have proposed an efficient and effective framework for vessel segmentation with good performance. This will be a powerful tool in analysis of vasculatures for management of a wide spectrum of vascular related diseases.

[3]`http://vampire.computing.dundee.ac.uk/vesselseg.html`

7. Acknowledgments

The project was supported by National Basic Research Program of China (2013CB328806), National Natural Science Foundation of China (81430039, 61572076), the Key Projects in the National Science & Technology Pillar Program (2013BAI01B01), National Hi-Tech Research and Development Program (2015AA043203), and China Postdoctoral Science Foundation Grant (2015M570940), the Key Laboratory of Photoelectronic Imaging Technology and System Beijing Institute of Technology Ministry of Education of China (2016OEIOF03).

8. References

[1] R. Achanta, A. Shaji, K. Smith, A. Lucchi, and P. Fua. Slic superpixels compared to state-of-the-art superpixel methods. *IEEE Trans. Pattern Anal. Mach.Intell.*, 34:2274–2282, 2012.

[2] B. Al-Diri, A. Hunter, and D. Steel. An active contour model for segmenting and measuring retinal vessels. *IEEE Trans. Med. Imag.*, 28:1488–1497, 2009.

[3] P. Bankhead, J. McGeown, and T. Curtis. Fast retinal vessel detection and measurement using wavelets and edge location refinement. *PLoS ONE*, 7:e32435, 2009.

[4] M. Barchiesi, S. H. Kang, T. M. Le, M. Morini, and M. Ponsiglione. A variational model for infinite perimeter segmentations based on Lipschitz level set functions: Denoising while keeping finely oscillatory boundaries. *Multiscale Model. Sim.*, 8:1715–1741, 2010.

[5] T. Chan and L. Vese. Active contours without edges. *IEEE Trans. Image Process.*, 10:266–277, 2001.

[6] L. Chen and S. Li. A semi-automatic method for vascular image segmentation. In *International Conference on Image and Graphics*, pages 12–15, 2011.

[7] M. Cheng, G. Zhang, N. Mitra, X. Huang, and S. Hu. Global contrast based salient region detection. In *Proceedings of the IEEE International Conference on Computer Vision and Pattern Recognition*, pages 409–416, 2011.

[8] U. Deepak, A. Chakravarty, and J. Sivaswamy. Visual saliency based bright lesion detection and discrimination in retinal images. In *Proc. IEEE Int. Sypm. Biomed. Imag.*, pages 1436–1439, 2013.

[9] B. Dizdaroglu, E. Ataer-Cansizoglu, J. Kalpathy-Cramer, K. Keck, M. Chiang, and D. Erdogmus. Level sets for retinal vasculature segmentation using seeds from ridges and edges from phase maps. In *Proc. IEEE Int. Workshop. Mach. Learn. Signal Process*, pages 1–6, 2012.

[10] M. Elad. Retinex by two bilateral filters. *Scale Space and PDE Methods in Computer Vision*, 3459:217–229, 2005.

[11] F. Frangi, Wiro J. Niessen, Koen L. Vincken, and Max Viergever Viergever. Multiscale vessel enhancement filtering. In *Med. Image Comput. Comput. Assist. Interv.*, volume 1496, pages 130–137, 1998.

[12] M. M. Fraz, P. Remagnino, A. Hoppe, B. Uyyanonvara, A. R. Rudnicka, C. G. Owen, and S. A. Barman. Blood vessel segmentation methodologies in retinal images - a survey. *Comput. Meth. Prog. Bio.*, 108:407–433, 2012.

[13] D. Gao, V. Mahadevan, and N. Vasconcelos. On the plausibility of the discriminant center-surround hypothesis for visual saliency. *Journal of Vision*, 8:1–18, 2008.

[14] X. Hou and L. Zhang. Saliency detection: A spectral residual approach. In *Proceedings of the IEEE International Conference on Computer Vision and Pattern Recognition*, pages 1–8, 2007.

[15] L. Itti, C. Koch, and E. Niebur. A model of saliency-based visual attention for rapid scene analysis. *IEEE Transaction on Pattern Analysis and Machine Intelligence*, 20:1254–1259, 1998.

[16] V. Jampani, J. Sivaswamy, and V. Vaidya. Assessment of computational visual attention models on medical images. In *Proc. Indian Conf. Comput. Vis. Graph. Imag. Process.*, pages 1–8, 2012.

[17] C. Kirbas and F. Quek. A review of vessel extraction techniques and algorithms. *ACM Comput. Surv.*, 36:81–121, 2004.

[18] G. Lathen, J. Jonasson, and M. Borga. Blood vessel segmentation using multi-scale quadrature filtering. *Pattern Recogn. Lett.*, 31:762–767, 2010.

[19] D. Lesagea and G. Funka-Leaa. A review of 3D vessel lumen segmentation techniques: Models, features and extraction schemes. *Med. Image Anal.*, 13:819–845, 2009.

[20] C Li, C Kao, J. Gore, and Z. Ding. Minimization of region-scalable fitting energy for image segmentation. *IEEE Trans. Image Process.*, 17:1940–1949, 2008.

[21] C. Li, C. Xu, M. Gui, and M.D. Fox. Distance regularized level set evolution and its application to image segmentation. *IEEE Trans. Image Process.*, 19:3243–3254, 2010.

[22] G. Luo, C. Opas, and M. Shankar. Detection and measurement of retinal vessels in fundus images using amplitude modified second-order Gaussian filter. *IEEE Trans. Biomed. Eng.*, 49:168–172, 2008.

[23] C. Lupascu, D. Tegolo, and E. Trucco. FABC: Retinal vessel segmentation using AdaBoost. *IEEE Trans. Inf. Technol. Biomed.*, 14:1267–1274, 2010.

[24] D. Mahapatra and Y. Sun. Mrf-based intensity invariant elastic registration of cardiac perfusion images using saliency information. *IEEE Trans. Biomed Eng.*, 58(4):991–1000, April 2011.

[25] D. Marin, A. Aquino, M.E. Gegundez-Arias, and J.M. Bravo. A new supervised method for blood vessel segmentation in retinal images by using gray-level and moment invariants-based features. *IEEE Trans. Med. Imag.*, 30:146–158, 2011.

[26] M. Martinez-Perez, A. Hughes, S.A. Thom, A.A. Bharath, and K.H. Parker. Segmentation of blood vessels from red-free and fluorescein retinal images. *Med. Image Anal.*, 11:47–61, 2007.

[27] A. Mendonça and A. C. Campilho. Segmentation of retinal blood vessels by combining the detection of centerlines and morphological reconstruction. *IEEE Trans. Med. Imag.*, 25:1200–1213, 2007.

[28] H. Narasimha, V. Mahadevan, J.M. Beach, and B. Roysam. Improved detection of the central reflex in retinal vessels using a generalized dual-Gaussian model and robust hypothesis testing. *IEEE Trans. Inf. Technol. Biomed.*, 12:406–410, 2008.

[29] M. Ng and W. Wang. A total variation model for retinex. *SIAM J. Imaging Sci.*, 4:345365, 2011.

[30] U. Nguyen, A. Bhuiyan, A.F. Laurence, and K. Ramamohanarao. An effective retinal blood vessel segmentation method using multi-scale line detection. *Pattern Recogn.*, 46:703715, 2013.

[31] J. Orlando and M. Blaschko. Learning fully-connected CRFs for blood vessel segmentation in retinal images. In *Med. Image Comput. Comput. Assist. Interv.*, pages 634–641, 2014.

[32] M. Palomera-Prez, M. Martinez-Perez, H. Bentez-Prez, and J.L. Ortega-Arjona. Parallel multiscale feature extraction and region growing: application in retinal blood vessel detection. *IEEE Trans. Inf. Technol. Biomed.*, 14:500–506, 2010.

[33] E. Ricci and R. Perfetti. Retinal blood vessel segmentation using line operators and support vector classification. *IEEE Trans. Med. Imag.*, 26:1357–1365, 2007.

[34] F. Rossant, R. Maddalena, A. Chavillon, I. Bloch, and M. Paques. A morphological approach for vessel segmentation in eye fundus images, with quantitative evaluation. *J. Med. Imaging. Health. Inf.*, 1:42–49, 2011.

[35] C. Sinthanayothin, J. Boyce, H. Cook, and T. Williamson. Automated localisation of the optic disc, fovea, and retinal blood vessels from digital colour fundus images. *Brit. J. Ophthal.*, 83:902–910, 1999.

[36] J. Soares and M. Cree. Retinal vessel segmentation using the 2D Gabor wavelet and supervised classification. *IEEE Trans. Med. Imag.*, 25:1214–1222, 2006.

[37] J. Staal, M.D. Abramoff, M. Niemeijer, M.A. Viergever, and B. van Ginneken. Ridge-based vessel segmentation in color images of the retina. *IEEE Trans. Med. Imag.*, 23:501–509, 2004.

[38] K. Sum and P. Cheung. Vessel extraction under non-uniform illumination: A level set approach. *IEEE Trans. Biomed. Eng.*, 55:358–360, 2008.

[39] K. Sun and S. Jiang. Local morphology fitting active contour for automatic vascular segmentation. *IEEE Trans. Biomed. Eng.*, 59:464–473, 2012.

[40] C. Wang, X. Chen. An efficient level set method based on multi-scale image segmentation and hermite differential operator. *Neurocomputing*, 188:90–101, 2016.

[41] S. Wang, Y. Yin, G. Cao, B. Wei, Y. Zheng, and G. Yang. Hierarchical retinal blood vessel segmentation based on feature and ensemble learning. *Neurocomputing*, 149, Part B:708–717, 2015.

[42] Y. Wang, Guangrong Ji, P. Lin, and E. Trucco. Retinal vessel segmentation using multiwavelet kernels and multiscale hierarchical decomposition. *Pattern Recogn.*, 46:2117–2133, 2013.

[43] X. You, Q. Peng, Y. Yuan, Y. Cheung, and Jia. Lei. Segmentation of retinal blood vessels using the radial projection and semi-supervised approach. *Pattern Recogn.*, 44:2314–2324, 2011.

[44] Y. Yuan, J. Wang, B. Li, and M. Meng. Saliency based ulcer detection for wireless capsule endoscopy diagnosis. *IEEE Trans. Med. Imag.*, 34(10):2046–2057, 2015.

[45] B. Zhang, L. Zhang, L. Zhang, and F. Karray. Retinal vessel extraction by matched filter with first-order derivative of Gaussian. *Comput. Biol. Med.*, 40:438–445, 2010.

[46] Y. Zhao and Y. Liu. A Retinex theory based points sampling method for mesh simplification. In *Proceedings of the 7th International Symposium on Image and Signal Processing and Analysis*, pages 230–235, 2011.

[47] Y. Zhao, Y. Liu, S. Harding, , and Y. Zheng. Retinal vessel segmentation: An efficient graph cut approach with retinex and local phase. *PLoS ONE*, page 10(4): e0122332, 2015.

[48] Y. Zhao, Y. Liu, Y. Wang, B. Wei, J. Yang, Y. Zhao, and Y. Wang. Region-based saliency estimation for 3d shape analysis and understanding. *Neurocomputing*, 197:1–13, 2016.

[49] Y. Zhao, I. J. MacCormick, D. Parry, S. Leach, N. Beare, S. P. Harding, and Y. Zheng. Automated detection of leakage in fluorescein angiography images with application to malarial retinopathy. *Sci. Rep.*, 5:e10425, 2015.

[50] Y. Zhao, I. J. MacCormick, D. Parry, S. Leach, N. Beare, S. P. Harding, and Y. Zheng. Automated detection of vessel abnormalities on fluorescein angiogram in malarial retinopathy. *Sci. Rep.*, 5:e11154, 2015.

[51] Y. Zhao, L. Rada, K. Chen, S. Harding, and Y. Zheng. Automated vessel segmentation using infinite perimeter active contour model with hybrid region information with application to retinal images. *IEEE. Trans. Med. Imag.*, 34:1797–1807, 2015.

[52] S. Zhou and Y. Gong. Active contour model based on local and global intensity information for medical image segmentation. *Neurocomputing*, 186:107–118, 2016.

2017-02-22

Saliency driven vasculature segmentation with infinite perimeter active contour model

Zhao, Yitian

Elsevier

Zhao Y, Zhao J, Yang J, Liu Y, Zhao Y, Zheng Y, Xia L, Wang Y, Saliency driven vasculature segmentation with infinite perimeter active contour model, Neurocomputing, Vol. 259, 11 October 2017, pp. 201-209

http://dx.doi.org/10.1016/j.neucom.2016.07.077